# LES of bifurcation and hysteresis in confined annular swirling flows

Mario Falese, Laurent Y.M. Gicquel, Thierry Poinsot

# LES of bifurcation and hysteresis in confined annular swirling flows

Mario Falese [a,*], Laurent Y.M. Gicquel [a], Thierry Poinsot [b]

[a] Centre Européen de Recherche et de Formation Avancée en Calcul Scientifique (CERFACS), 31057 Toulouse, France
[b] Institut de Mécanique des Fluides de Toulouse (IMFT), 31100 Toulouse, France

A B S T R A C T

This paper presents a LES based study of two swirling confined jet configurations corresponding to an aeronautical injection system. The objectives are to demonstrate that LES codes become sensitive to numerical parameters (grid, SGS model) in such cases and that this is due to the fact that these flows are close to bifurcating conditions because of the presence of swirl and confinement walls. To demonstrate this, in the first configuration ('full swirler'), the swirler/plenum ensemble is computed while only the swirler without plenum is computed in the second ('adjustable swirler'): this simplification allows to vary swirl continuously and explore bifurcation diagrams where the control parameter is the mean swirl number. These numerical results are compared to a similar study performed experimentally by Vanierschot and Van den Bulck (2007) [1]. They confirm that certain confined swirling flows are intrinsically submitted to bifurcations. In the context of LES this leads to a large sensitivity of the simulation results to numerical parameters, a property which is not observed in most other non swirling or non confined situations.

*Keywords:*
LES
Swirl flows
Bifurcation
Hysteresis
Numerical simulations
Swirling jets
Aeronautical injector

## 1. Introduction

The objectives of this work are (1) to study bifurcation in confined swirling flows, typically swirlers used in combustion system and (2) to indicate specific aspects of LES methods to which careful attention must be paid for a successful simulation of an industrial swirling flow. Swirling jets are essential elements of many combustion chambers and lead to complex flows which control the fuel atomization, the shape of the recirculating zone produced in front of the swirler and ultimately a large part of the engine performances. Experimentalists know that bifurcation is a common feature in many swirling flows where multiple instabilities take place [3]. The most common of them is vortex breakdown [4,5], which occurs when reverse flow takes place along the jet axis [6] because of the adverse pressure gradient induced by the conservation of circulation and the jet expansion [4], as first proposed by Hall [7]. Seven different types of vortex breakdown have been identified depending on the swirl and Reynolds number [3] but there are numerous parameters ranges for which "two forms (or more) can exist and transform spontaneously into each other" [5]. Swirl intensity is one of the parameters controlling transition between flow states and its effects will be analyzed here using LES, focusing the investigation on an aeronautical swirl injector. Two geometries are analyzed in this paper; in the first, named full swirler, the plenum (located upstream of the injector) and the swirler passages are included in the simulation domain (Fig. C.1). Results of the full swirler case show that LES can bifurcate depending on the grid resolution inside the radial swirler, under the same inflow conditions. This property is observed exactly in the same manner for the two LES codes used here: AVBP [8,9] and YALES2 [10] (a compressible and an incompressible LES solver respectively).

In the second geometry, named adjustable swirler (Fig. C.1), the simulation domain, extracted from the full geometry of the full swirler case, starts downstream of the swirler vanes. The three counter-rotating swirlers, which together form the swirl injector, are replaced by a set of boundary conditions (B.C.s) in order to vary the swirl intensity as desired. This modification allows to transform the original, swirl injector into an adjustable swirl device which can be used to change swirl over a wide range and to explore the resulting flow topologies. The jet states generated in the adjustable swirler case show common, peculiar, properties with the experimental results of Vanierschot and Van den Bulck [1]. Even if the exact limits of the different states and the hysteresis patterns differ (as a consequence of the different geometries), both the present LES of an aeronautical swirler and the simpler configuration of Vanierschot and Van den Bulck [1], exhibit similar bifurcations controlled by the swirl level and induced by the presence of confinement walls. This suggests that LES of confined swirling flows can be difficult because of their natural sensitivity to small swirl level variations: in the real world, this sensitivity leads to bifurcations and hysteresis mechanisms; in LES, it explains why simulation results of swirling flows are very sensitive to small

* Corresponding author. Tel.: +33 0561193109.
*E-mail address:* falese@cerfacs.fr (M. Falese).

**Nomenclature**

| | | | |
|---|---|---|---|
| $D_0$ | jet characteristic diameter [m] | $P$ | pressure [kg/s$^2$/m] |
| $R_0$ | jet characteristic radius [m] | $P_{atm}$ | atmospheric pressure [kg/s$^2$/m] |
| $U_0$ | jet characteristic speed [m/s] | $P_D$ | normalized subpressure [–] |
| $x$, $X$ | axial position [m] | $y^+$ | nondimensional wall distance [–] |
| $r$, $R$ | radial position [m] | $Pope$ | Pope criterion [2] [–] |
| $S$ | swirl number [–] | $k_{res}$ | resolved, turbulent kinetic energy [m$^2$/s$^2$] |
| $u_a$ | axial velocity [m/s] | $k_{sgs}$ | SGS, turbulent kinetic energy [m$^2$/s$^2$] |
| $u_\theta$ | tangential velocity [m/s] | $\nu_t$ | turbulent viscosity [m$^2$/s] |
| $u_r$ | radial velocity [m/s] | $C_m$ | SGS model constant [–] |
| $U$ | jet velocity [m/s] | $C_M$ | constant [–] |
| $\rho$ | density [kg/m$^3$] | $\tilde{u}$ | filtered velocity [m/s] |
| $\Delta$ | grid size [m] | $D_m(\tilde{u})$ | differential operator [1/s] |
| $T$ | temperature [K] | | |

details of the numerical setup (mesh, SGS model, boundary conditions) and require much more attention. Section 2 first recalls evidences of bifurcation in swirling flows obtained experimentally and presents a jet states classification based on flow properties. Section 3 describes the swirler investigated using LES here in the full swirler case and presents the effects of bifurcation observed for this flow. The source of these bifurcations is identified in Section 4, where the adjustable swirler is computed and a bifurcation diagram depending on the swirl number is constructed. Results of Section 4 shows that LES is sensitive to numerical parameters in the full swirler case because the jet has a swirl number corresponding to an hysteresis zone, which is captured in the adjustable swirler LES.

## 2. Bifurcation in confined swirling flows: experimental evidence

This section discusses flow states which can appear in confined swirling flows because of the proximity of solid boundaries. Above a critical swirl strength, confinement walls alter (the expansion angle of the jet, which can attach to the sidewalls and behave) like a radial jet, a phenomenon similar to the Coanda effect [12]. The critical swirl number at which this transition takes place is dependent on the nozzle geometry as several phenomena such as separation of the jet, Coanda effect and jet expansion angle all play a role. In Chedaille et al. [13], three different swirling jet configurations appear depending on the nozzle opening angle or on the expansion rate of the divergent nozzle. Similar jet configurations and recirculation zones are reported by Beer and Chigier [14], in a qualitative manner and more recently by Vanierschot and Van den Bulck [1]. The experiment of Vanierschot and Van den Bulck [1], provides a quantitative analysis of a flow with variable swirl and it will be used as a reference example to classify flow states. Vanierschot and Van den Bulck [1], investigate the influence of swirl on an annular jet with a stepped-conical expansion ($Re$ = 11,000), identifying four, distinct flow states.

The first two states identified by Vanierschot and Van den Bulck [1], are named here, "Un-broken axial jet" (UJ) and "free Axial Jet" (AJ) (Fig. C.2). UJ states are obtained when $S < 0.4$ while AJ states appear for $S \geq 0.4$, where the swirl number $S$ is defined by:

$$S = \frac{\int_A \rho u_a u_\theta r \, dA}{R_0 \int_A \rho u_a u_a \, dA}. \quad (1)$$

At $S = 0.4$, vortex breakdown takes place in this configuration. The transition between the "Axial Jet" and the "Weak axial Jet" (WJ), as named here, and the transition between the WJ and the "Blasted Breakdown jet" (BB), as named here, take place as follows (Fig. C.3).

First, increasing the swirl number up, from state AJ, to the second critical threshold of $S = 0.6$, the flow bifurcates to the WJ state. The AJ–WJ transition is the result of the attachment of the jet to the side walls of the nozzle (Fig. C.2) which causes a widening of the expansion angle of the jet and the creation of a "corner recirculation zone" between the jet and the diffuser walls [15]. This bifurcation is characterized by an abrupt expansion of the Central Toroidal Recirculation Zone (CTRZ) which doubles its diameter (Fig. C.2). At the same time, the azimuthal velocity, the sub-pressure in the CTRZ and turbulence levels, decrease. Because of hysteresis, the WJ state remains stable even when swirl is decreased back to values which are lower than the transition point AJ–WJ ($S = 0.6$). At $S = 0.5$ (transition WJ–BB), the jet "attaches to the horizontal wall of the infinite expansion and a purely radial jet is formed" [1], a phenomenon also known as the Coanda effect. A third bifurcation takes place: the recirculation zone widens even more (its "eye" has disappeared from Fig. C.2); sub-pressure, tangential velocity

**Table C.2**
Imposed boundary values for LES of the full swirler case.

| | | |
|---|---|---|
| *Swirler B.C.s (Fig. C.4)* | | |
| B.C. name | Imposed property | Target value |
| Cooling film | Mass flow – $T$ | 30.3 [g/s] to 270 K |
| Plenum inlet | Mass flow – $T$ | 102.12 [g/s] to 270 K |
| *Far field B.C.s (Fig. C.4)* | | |
| B.C. name | imposed property | Target value |
| Coflow | Speed – $T$ | 1 [m/s] to 270 K |
| Outlet | Pressure | 99,000 [Pa] |
| Walls | Adherence, impermeability, adiabaticity | |

**Table C.1**
Summary of the characteristics of the three different states (AJ–WJ–BB) documented in [1] after vortex breakdown. $R_v$ indicates the approximate radial position of the "eye" of the CTRZ while $P_D$ is the subpressure normalized by the jet kinetic energy, $P_D = \frac{P_{atm}-P}{0.5\rho U_0^2}$.

| Flow state | CTRZ size | Normalized subpressure | CTRZ tangential velocity | CTRZ Reynolds stresses |
|---|---|---|---|---|
| AJ | $R_v < 0.5$ | $1.4 < P_D < 0.8$ | High | High |
| WJ | $0.5 < R_v < 1$ | $P_D < 0.4$ | Moderate | Moderate |
| BB | $R_v \gg 1$ | $P_D = 0$ | Zero | Zero |

**Table C.3**
Summary of the characteristics of the full swirler case simulations of Fig. C.8. Simulation names indicate the code (AVBP [8,9] or YALES2 [10]) and the grid (basic vs. optimized, OPT) used.

| LES name | *S*, Eq. (1) inner axial jet | *S*, Eq. (1) outer axial jet | *S*, Eq. (1) radial swirler jet | Flow state |
|---|---|---|---|---|
| AVBP-BASIC | 0.12 | −0.60 | 0.82 | BB |
| YALES-BASIC | 0.12 | −0.58 | 0.80 | BB |
| AVBP-OPT | 0.12 | −0.61 | 0.76 | AJ |
| YALES-OPT | 0.12 | −0.58 | 0.74 | AJ |

**Table C.4**
First set of LES of the adjustable swirler case.

| LES name | S (Eq. (1)) inner/outer jet | S (Eq. (1)) radial jet | Jet configuration |
|---|---|---|---|
| Basic | 0.12/−0.4 | 0.75 | AJ |
| High | 0.12/−0.4 | 0.84 | BB |

**Table C.5**
Characteristics of LES of Path A and B.

| LES name | *S* (Eq. (1)) radial jet | Initial condition | Jet configuration |
|---|---|---|---|
| P1_U | 0.84 | Basic | WJ → BB |
| P1_D | 0.75 | High | BB |
| P2_D | 0.60 | P1_D | AJ |
| P3_D | 0.75 | P2_D | AJ |

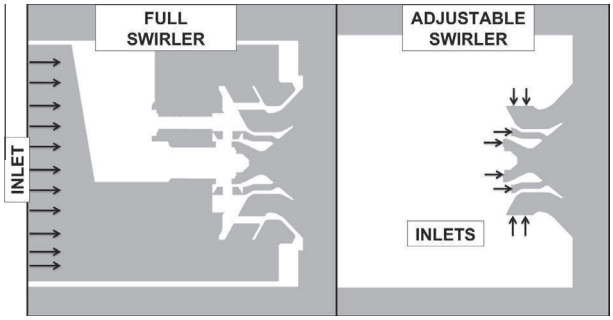


**Fig. C.1.** Full and adjustable swirler configurations. Arrows represent inlet boundary conditions.

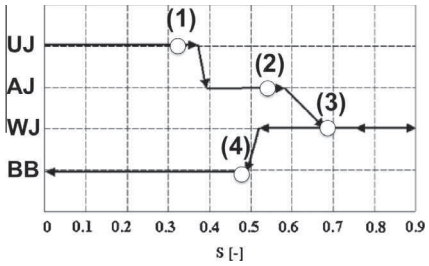


**Fig. C.3.** Transition map of Vanierschot and Van den Bulck [1]. The different flow states are plotted against the swirl number *S*. The four states of Fig. C.2 (1–4) are added on the diagram.

and turbulent kinetic energy drop to zero close to the flow centerline (where the vortex breakdown, in the WJ state, is located). The characteristics of the three flow states of interest for the current study are summarized in Table C.1: after each transition (AJ–WJ–BB) CTRZ expands, tangential velocity and subpressure (which are inter-related) diminish, turbulence intensity reduces. For a swirl number of 0.3, for example, two very different states (UJ and BB) can be obtained (Fig. C.3).

Bifurcation and hysteresis described in [1] are the result of a variety of mechanisms (jet expansion angle related to the swirl level, jet attachment to the nozzle walls, dynamics of the corner recirculation zone [15]) which are configuration dependent.

## 3. LES of an aeronautical swirl injector: full swirler case

The first part of the present work focuses on mesh effects on LES of an industrial swirling flow, a configuration more complex than the Vanierschot geometry [1]. To make sure that conclusions are not code dependent, two completely different LES solvers have

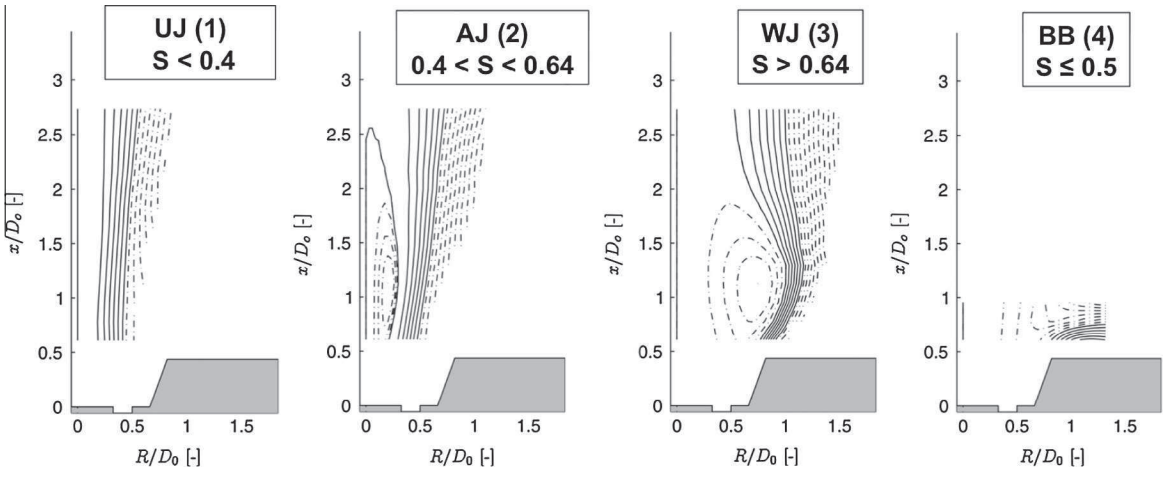


**Fig. C.2.** Experimental results of Vanierschot and Van den Bulck [1]: streamlines for four different flow states. Solid lines correspond to the jet boundaries and dashed-dotted lines are recirculation zones. Swirl number exact values are from left to right: $S = 0.335, 0.56, 0.69, 0.5$. The flow states named here UJ, AJ, WJ and BB were originally named [1]: "closed jet flow", "open jet low swirl flow", "open jet high swirl flow" and "Coanda jet flow" respectively.

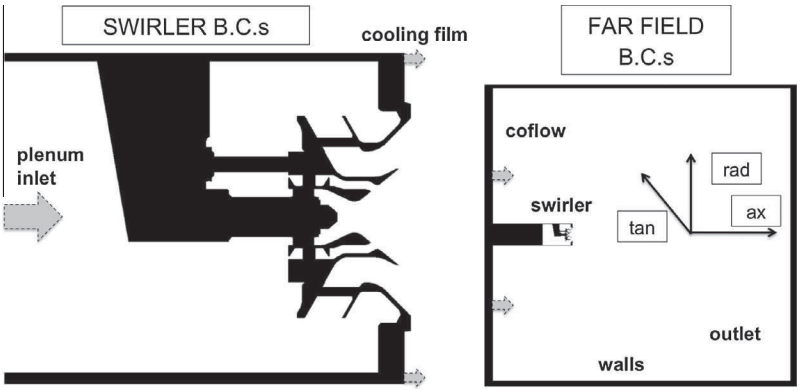


**Fig. C.4.** Aeronautical swirler boundary conditions for the full swirler case. Arrows indicates inlets. The right picture specifies the flow directions (ax = axial, rad = radial and tan = tangential) in cylindrical coordinates, where the axial direction corresponds to the axis of symmetry of the cylindrical box used to mimic open atmosphere.

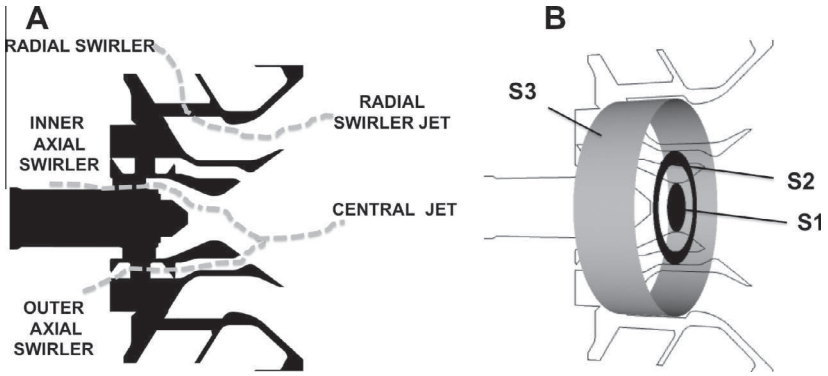


**Fig. C.5.** full swirler case. (A) Swirler passages and jets. (B) Measurement surfaces for the swirl numbers Eq. (1). *S*1 and *S*2 are the measurement surfaces for the two co-axial jets. *S*3 for the radial jet.

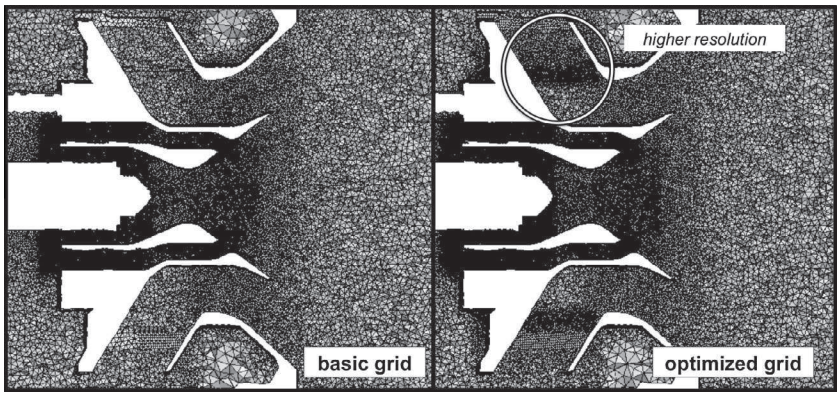


**Fig. C.6.** Full swirler case, basic and optimized grids.

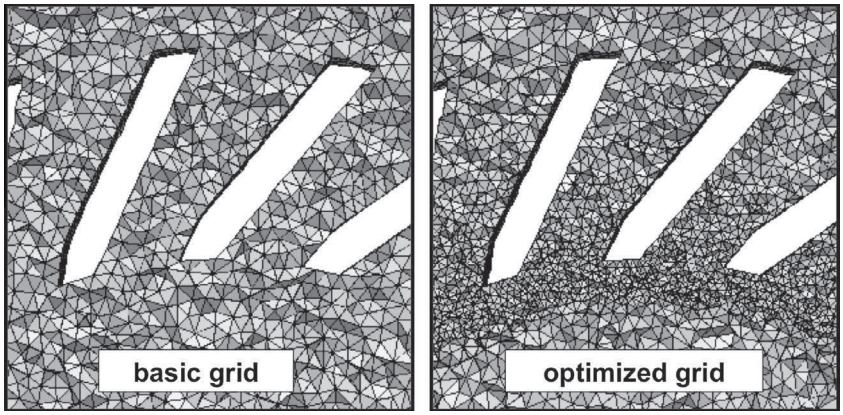


**Fig. C.7.** Full swirler case, basic and optimized grids, zoom at the radial swirler.

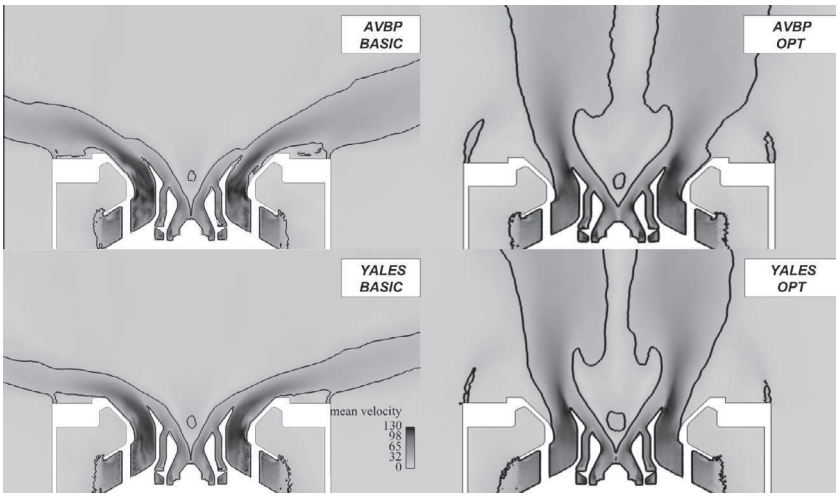


**Fig. C.8.** Flow fields of the full swirler case LES of Table C.3. The jet bifurcates in both codes (AVBP [8,9] and YALES2 [10]) depending on the grid used (basic vs. optimized grid, Figs. C.6 and C.7). In black, iso-velocity line ($U = 20$ [m/s]).

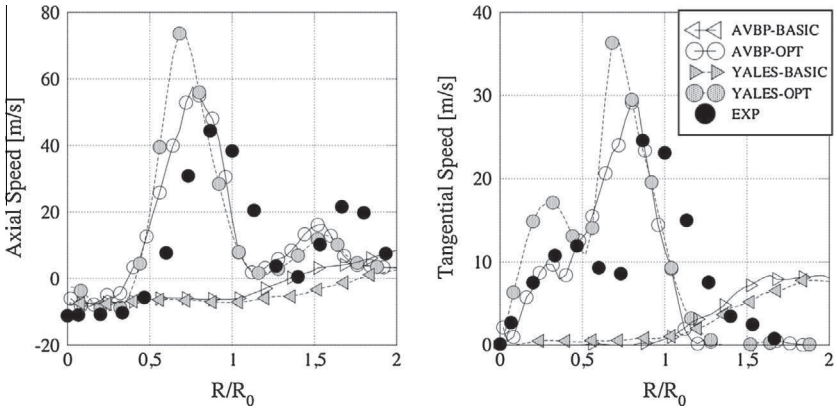


**Fig. C.9.** Flow velocities plotted against normalized radial positions ($R/R_0$) of LES of the full swirler case, Table C.3. Measurement are taken $0.5R_0$ downstream of the swirler ending plate.

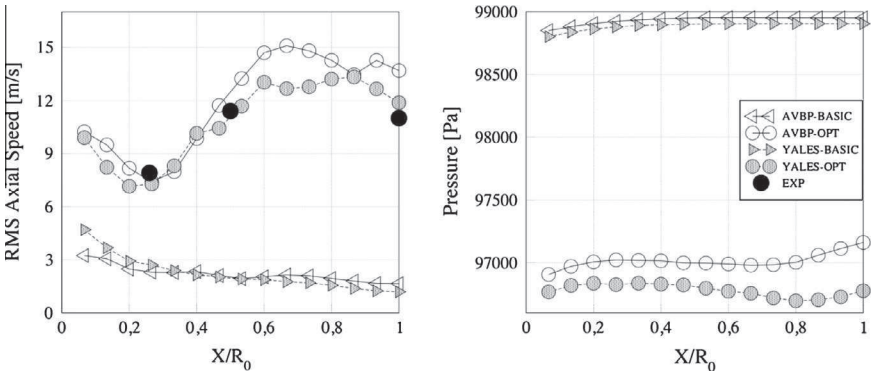


**Fig. C.10.** Axial velocity RMS and pressure distribution measured along the centerline of the geometry. Results are plotted against normalized axial distance ($X/R_0$) from the swirler ending plate, for the full swirler case simulations, Table C.3. Experimental data are available only for RMS values.

been tested: AVBP [8,9] and YALES2 [10], a compressible and an incompressible LES solver respectively, whose characteristics are recalled in Appendix B at the end of this paper. The configuration corresponds to an aeronautical liquid fuel injector which has been experimentally investigated at ONERA (Office National d'Etudes et Recherches Aerospatiales) in the framework of the European project KIAI (Knowledge for Ignition Acoustics and Instabilities). It consists of "a pilot injection system (Fig. C.4) surrounded by two counter-rotating axial swirlers and a multipoint injection system, surrounded by a radial swirler" [11]. Experimental measurements were taken in open atmosphere at 99,000 [Pa] and 270 K. The injector was fed with air. The mass flow rate studied

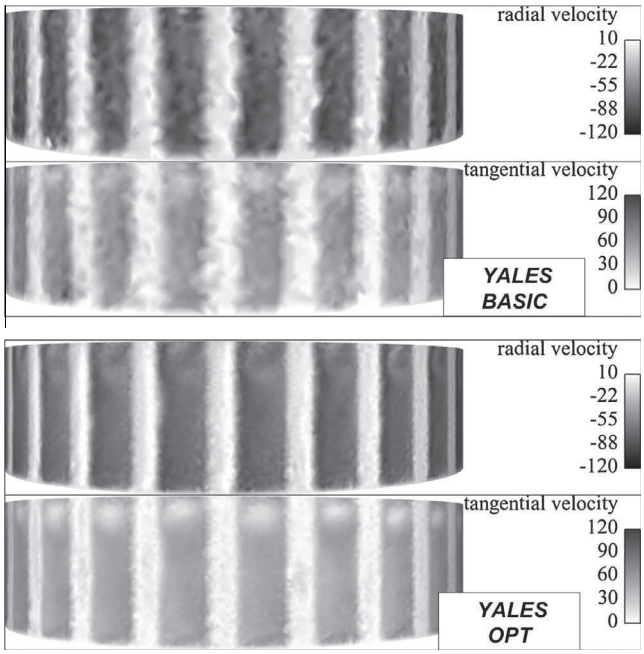


**Fig. C.11.** Mean radial and tangential velocities ([m/s]) on surface S3 (Fig. C.5) for LES YALES-BASIC and YALES-OPT of Table C.3. The mean flow speed is more irregular on the basic grid (top) than on the optimized grid (bottom) because of the different grid resolution in this zone.

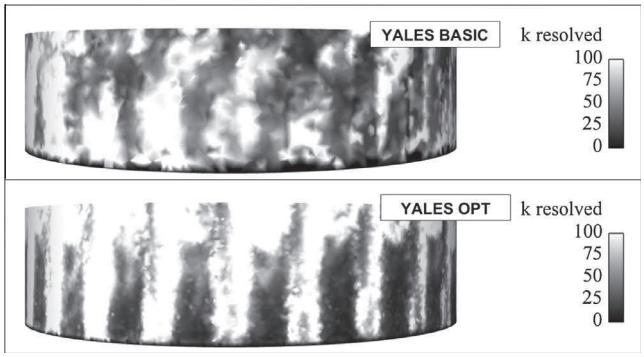


**Fig. C.12.** Resolved turbulent kinetic energy for LES YALES-BASIC and YALES-OPT of Table C.3.

here is 138 [g/s], introduced via an upstream plenum; the pressure drop corresponding to these conditions is 4800 [Pa]. Two passages connect the plenum to the open atmosphere: the swirler, which is explicitly resolved in LES; a cooling film at the periphery of the injector, which is reproduced using a boundary condition (Fig. C.4).

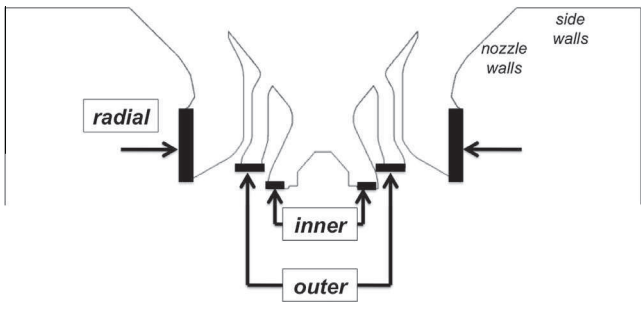


**Fig. C.13.** Domain of the adjustable swirler case and boundary conditions.

The swirler is fed by the plenum inlet shown in Fig. C.4, while the amount of mass flow rate evacuated by the cooling film is obtained from the permeability measurements of ONERA. The Reynolds number of the jet is 75,000, considering a jet speed $U_0 = O(75)$ [m/s], a characteristic length scale (size of the annular flow passage) of $O(10)$ [mm] and a kinematic viscosity of $O(10^{-5})$ [$m^2/s$]. The swirl number is measured before jets merge into common structures (Fig. C.5). Note that the swirl number of the radial swirler jet, evaluated on surface S3 of Fig. C.5B, is simply a measure of the angular momentum introduced into the flow by the radial jet for a given mass flow rate, since radial velocity is used in Eq. (1) instead of axial velocity. In order to mimic open atmosphere, the swirler is placed inside a cylindrical box ("far field" in Fig. C.4) with a diameter and a streamwise elongation of 24 and 25 swirler diameters respectively ($25D_0 = 1.5$ [m]) (Fig. C.4). Here, another set of boundary conditions is set up: the simulation outlet, with an imposed pressure of 99,000 [Pa]; an inlet coflow with an imposed velocity of 1 [m/s] (1.3% of $U_0$); solid walls at the periphery of the box. In the current analysis, the zone upstream of the injector is included (Fig. C.4) and the largest flow structures generated by the jet in the cylindrical box are explicitly resolved. To test the effects of the coflow, a simulation was performed imposing a higher streamwise velocity (10 [m/s]) for simulation high of Section 4: the jet is not modified, confirming, as shown in [16], that the coflow speed has no major influence on the flow structure. Finally, all solid boundaries present in the full swirler configuration are imposed as adherent, impermeable, adiabatic walls (Table C.2). Imposed boundary values are the same in both codes (AVBP [8,9] and YALES2 [10]).

Two meshes are used for the full swirler case, named basic and optimized grids in Fig. C.6: they contain 14,081,708 and 15,873,485 tetrahedra respectively. The basic and optimized grids have the same resolution except in the radial swirler (Fig. C.7). The optimized grid was generated from the analysis of the characteristics of the radial jet (Fig. C.5) in the basic grid. The radial jet showed a variation of $O(10\%)$ of the swirl level changing the SGS model (these results are not shown here) which suggested a localized mesh refinement in this zone, inside the radial swirler.

Four simulations are performed in the full swirler case (Table C.3) each of them initialized using a zero velocity flow field. Results show that the two LES codes behave similarly and that both predict results which depend on the grid: with the optimized grid, an axial jet (AJ) in which the flow detaches from the nozzle and is mainly axially oriented (Fig. C.8, right); with the basic grid, a Blasted Breakdown jet (BB), with the jet following the geometric curvature of the device (Fig. C.8, left). Note that the detachment/attachment dynamics of the jet from the nozzle walls are crucial to predict the flow state and require a fine grid resolution to be properly simulated.

As in [1], the AJ state is characterized by a recirculation zone smaller than one injector diameter and a high tangential velocity (Fig. C.9), a high level of turbulent activity and a high subpressure ($P_D \approx 0.56$) close to the injector orifice (Fig. C.10). On the contrary, the BB state is characterized by a wider recirculation zone and by (inside the CTRZ) a zero tangential velocity, a negligible turbulent activity and sub-pressure (Figs. C.9 and C.10).

Obviously, both AJ and BB states can appear as a function of the local grid resolution, basic vs. optimized grid see Fig. C.7, in the results of both LES codes, AVBP [8,9] and YALES2 [10]. The differences between the two codes are visualized in Fig. C.8, and quantified in terms of the velocity profiles in Fig. C.9. They are negligible compared to the bifurcation induced by the local grid resolution. Experimental data fit quite well the velocity profiles and RMS distribution of the AJ state (Figs. C.9 and C.10) while results associated to the BB state are clearly very different from the

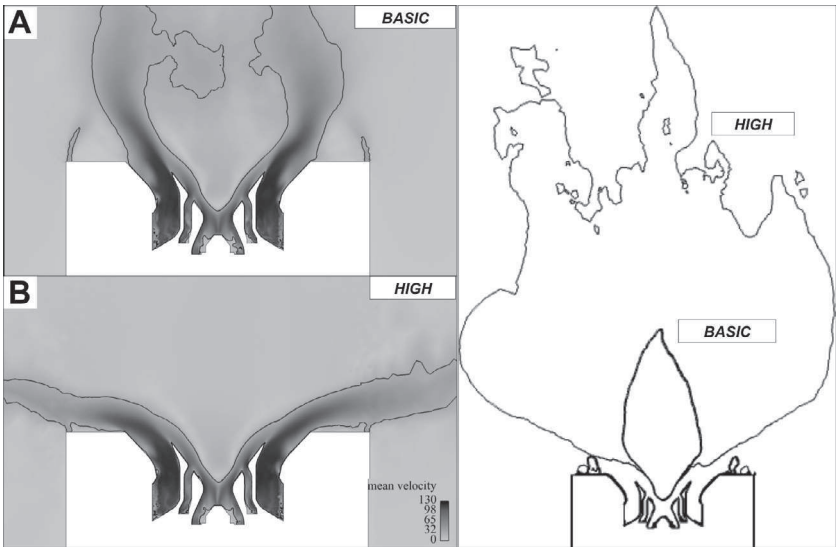


**Fig. C.14.** A-B: flow fields and velocity isoline ($U = 20$ [m/s]) of simulations basic and high of Table C.4. CTRZs lines (zero axial velocity isoline) of these simulations are plotted in the right picture.

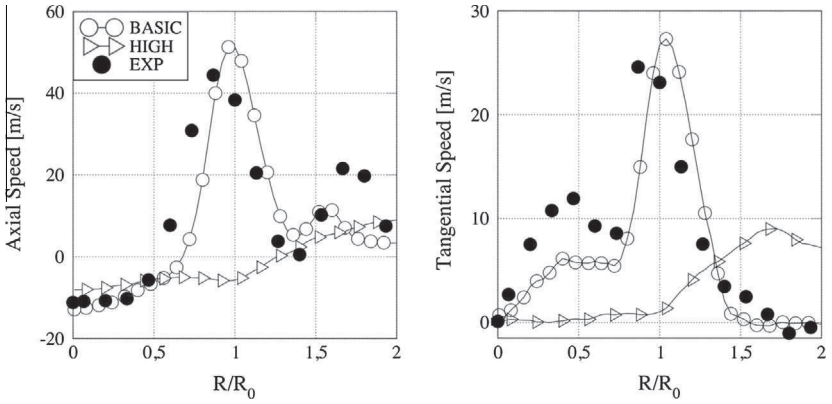


**Fig. C.15.** Flow velocities plotted against normalized radial positions for simulations basic and high of Table C.4. Measurement are taken $0.5R_0$ downstream of the swirler ending plate.

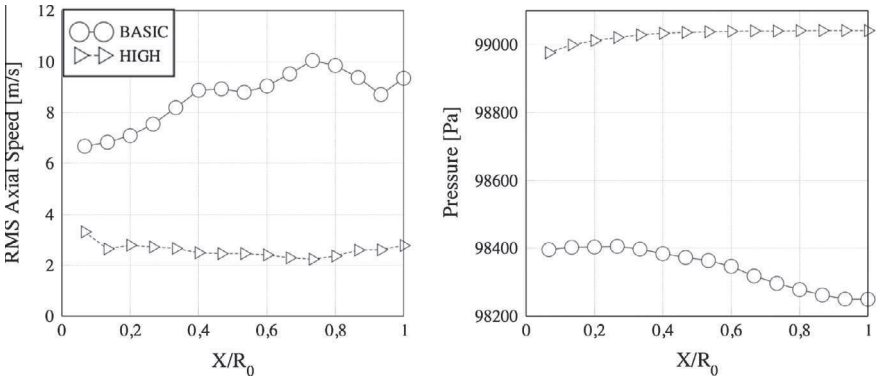


**Fig. C.16.** Axial velocity RMS and pressure distribution measured along the centerline of the geometry. Results are plotted against normalized axial distance ($X/R_0$) from the swirler ending plate for simulations basic and high of Table C.4.

experimental data. LES captures two flow states here (AJ and BB) while the experiment is showing only an AJ state.

An interesting observation in Table C.3 is that state BB is obtained in both codes for a swirl number of $S = 0.8$–$0.82$ (measured in Section S3 of Fig. C.5), while state AJ is obtained for a smaller swirl $\approx 0.76$. This suggests a possible explanation for the sensitivity of the flow to the grid: on the optimized grid the flow field computation leads to a smaller swirl number of the radial jet (downstream of the swirler vanes) and this change leads to an AJ state. This explanation makes sense only if a small variation of swirl

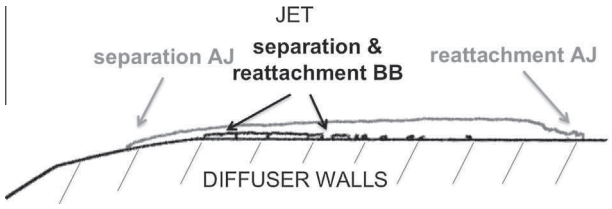


**Fig. C.17.** Jet separation and reattachment inside the nozzle for LES of Table C.4. The jet dynamics are made evident by the zero velocity isoline in the streamwise direction. Grey line, LES basic in the AJ state, Black line, LES high in the BB state.

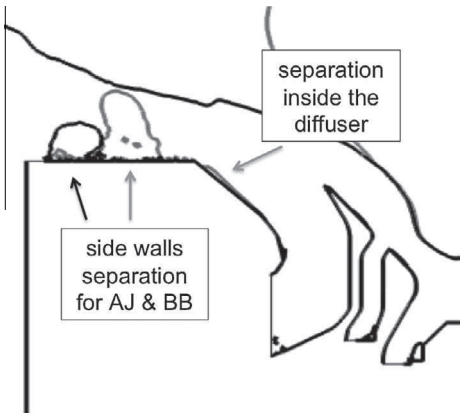


**Fig. C.18.** Jet separation and reattachment to the side walls for LES of Table C.4. The jet dynamics are made evident by the zero velocity isoline in the streamwise direction. Grey line, LES basic in the AJ state, Black line, LES high in the BB state.

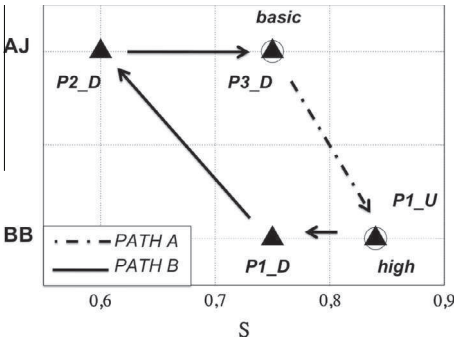


**Fig. C.19.** Transition map of the aeronautical swirler, adjustable swirler case. Circles are LES of path A (which starts with LES basic) while black triangles are LES of path B (which starts with LES high). The hysteresis loop is closed.

can trigger a large jet re-configuration, something that is possible only if the flow conditions are close to critical.

The dependency of the swirl number of the radial jet on the mesh resolution inside the radial swirler (i.e. using the basic or the optimized mesh of Fig. C.6) can be explained as follows. The swirl number measured inside each of the vanes of the radial swirler (measured 3 [mm] upstream of surface S3 of Fig. C.5, before the vanes converge and generate a single flow) is $S = 0.71$ for all simulations of Table C.3: here the swirl number is fully determined by the geometry of the flow passage. Only downstream, on surface S3 (Fig. C.5) where all vanes merge, the swirl number does change depending on the mesh used.

Here (see Fig. C.11 where the mean flow of LES YALES-OPT and YALES-BASIC on surface S3 are shown), the flow speed varies from 100 [m/s] in the core of one jet, to zero, because of the solid boundary, and again to 100 [m/s] because of the neighboring jet, in less than 5 [mm]. This large velocity gradient is challenging for LES: while the optimized mesh is sufficiently refined to simulate this configuration (see Fig. C.11 bottom where the mean flow looks regular and the backflow behind each swirler vane is distinct from the main stream), the basic mesh is not (see Fig. C.11 top and Fig. C.12). As a consequence, mesh resolution affects the mean velocity profile causing the swirl number of the jet to differ when the optimized mesh is replaced with the basic mesh.

Additional results (not shown here) show that a similar bifurcation (AJ–BB), appears in the LES with the basic mesh when the SGS model is changed, replacing SIGMA [17], with Dynamic Smagorinsky [18], for instance: two flow states appear above and below the supposed critical value of $S = 0.77—0.79$, on both codes (AVBP [8,9] and YALES2 [10]). The SIGMA model causes a high swirl level in the radial jet and a consequent BB state, while the Dynamic Smagorisnky model causes a low swirl level in the radial jet and an AJ state. The dependency on SGS model is due to the different amount of turbulent viscosity generated by the two models: SIGMA generates less turbulent viscosity than the Dynamic Smagorinsky model in the wakes of the radial swirler vanes. The turbulent viscosity generated by the SGS model interacts with the velocity field, damping the turbulence generated by the jet-to-jet interaction shown for instance in Fig. C.12. The overall effect is a modification of the mean velocity profile (determined by the amount of resolved turbulence which spreads momentum toward the different jet directions) so a variation of the swirl number which now depends on the turbulent viscosity level.

To clarify the dependency of the jet state to the amount of swirl of the flow, a modified swirler geometry is tested in LES (Section 4) where the simplification of the geometry allows to change swirl levels easily while keeping all numerical parameters constant.

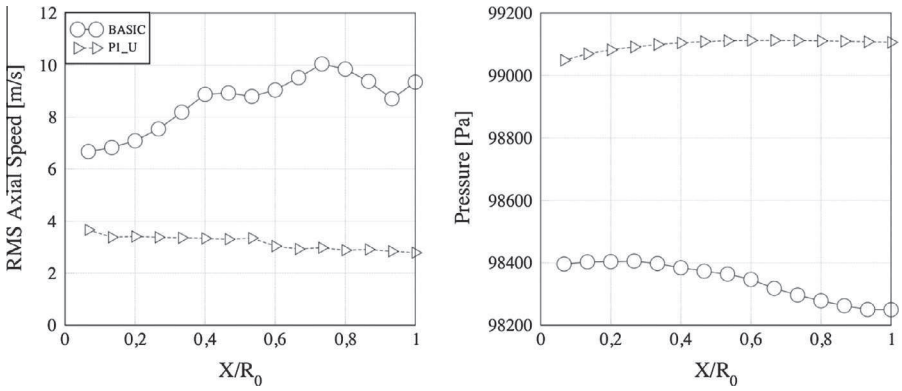


**Fig. C.20.** Axial velocity RMS and pressure distribution measured along the centerline of the geometry. Results are plotted against normalized axial distance ($X/R_0$) from the swirler ending plate, for simulations of path A, Table C.5.

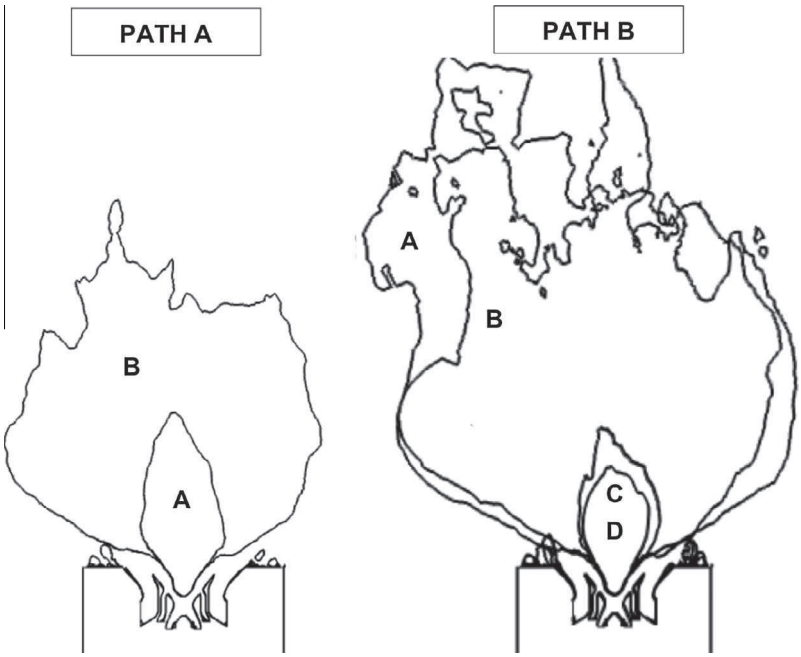


**Fig. C.21.** Path A: CTRZs of LES basic (A), *P*1_*U* (B). Path B: CTRZs of LES high (A), *P*1_*D* (B), *P*2_*D* (C), *P*3_*D* (D).

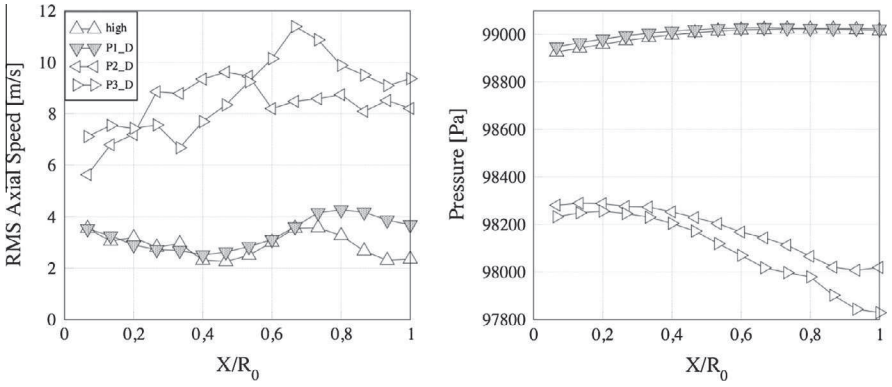


**Fig. C.22.** Axial velocity RMS and pressure distribution measured along the centerline of the geometry. Results are plotted against normalized axial distance ($X/R_0$) from the swirler ending plate, for simulations of path B, Table C.5.

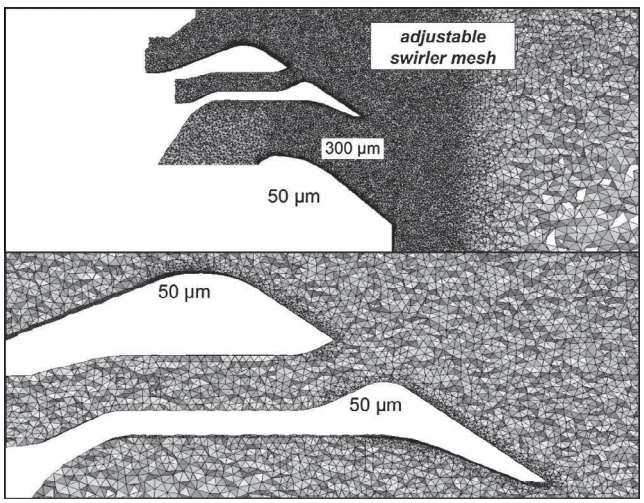


**Fig. C.23.** Adjustable swirler case mesh, zoom at the swirler.

## 4. LES of an aeronautical swirl injector with adjustable swirl: adjustable swirler case

This part is dedicated to the verification of the hypothesis presented in Section 3, namely that the swirled flow studied in Section 3 is close to critical conditions and that swirl is the main control parameter. The mesh and the numerical settings (all

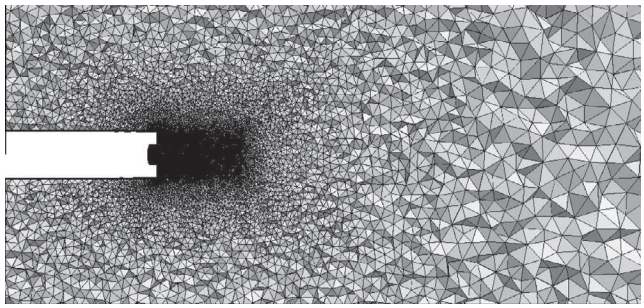

**Fig. C.24.** Adjustable swirler case mesh, far field.

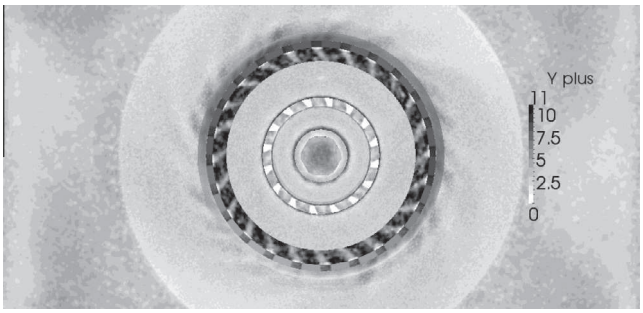


**Fig. C.25.** Mean $y^+$ values for LES basic of Section 4. The swirler surface is seen from the open atmosphere.

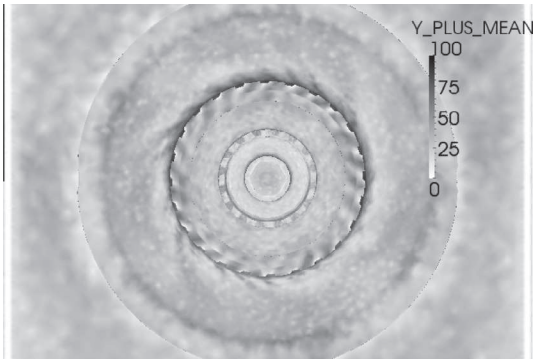


**Fig. C.26.** Mean $y^+$ values for LES YALES-OPT of Section 3. The swirler surface is seen from the open atmosphere.

simulations are performed with YALES2 [10]) are kept constant while the inlet conditions are varied in order to explore various swirl levels. To be able to modify the level of swirl, the original set up is modified and LES are conducted on a simpler geometry (Fig. C.13): the three swirlers, which determine the amount of swirl in the flow, and the upstream plenum are removed and replaced by inlets patches with adjustable swirl (Fig. C.13). As a result, the original swirl injector is transformed into an adjustable swirl device.

A similar methodology was used in [19] by imposing constant velocities at the swirler inlet. Here, the tangential velocity component of the "radial" B.C. (Fig. C.13) will also be varied in order to modify swirl. The cylindrical box used to mimic open atmosphere is the same as in the full geometry case while the mesh characteristics are shown in Appendix A. Since the domain is smaller, the mesh used for the adjustable swirler case is significantly finer and tests (not shown here) prove that results do not depend on the mesh for this case.

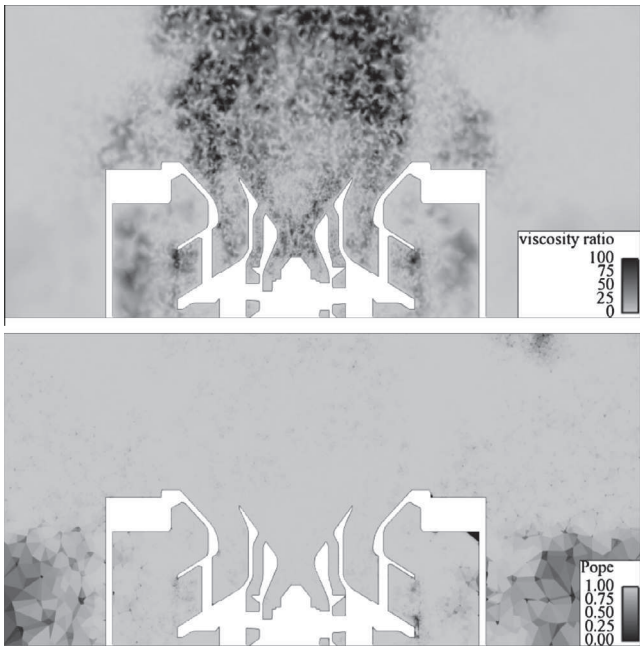


**Fig. C.28.** Snapshots of ratio of turbulent over laminar viscosity and Pope criterion, Eq. (A.1), for LES YALES-OPT of Section 3.

Two simulations are tested where the radial jet swirl number is varied. The swirl introduced by the inner and outer jets are kept constant ($S = 0.12$ and $S = 0.4$ respectively). The first simulation (basic) uses a swirl number of the radial jet similar to simulation AVBP-OPT or YALES-OPT; the second (high), uses a swirl number 10% higher ($S = 0.84$). Each simulation is initialized using a zero-velocity flow field. The characteristics of these two simulations are summarized in Table C.4, while their flow fields and CTRZs are shown in Fig. C.14.

The flow configuration of the basic case is characterized by a CTRZ smaller than one injector diameter (Fig. C.14), a high tangential velocity (Fig. C.15), a high sub-pressure ($P_D \approx 0.44$) and high turbulence intensity inside the CTRZ (Fig. C.16). On the contrary, the flow configuration of the high case is characterized by a CTRZ which is several injector diameters wide (Fig. C.14), a strong reduction of tangential velocity inside the CTRZ (Fig. C.15) and a reduced sub-pressure ($P_D \approx 0$) as well as a negligible turbulence intensity inside the CTRZ (Fig. C.16). The jet of basic LES is therefore in the AJ state while the jet of the high case is in the BB state: an increase of 10% of the swirl number of the radial swirler jet (from $S = 0.75$ to $S = 0.84$) is enough to induce a bifurcation of the flow from AJ to BB states.

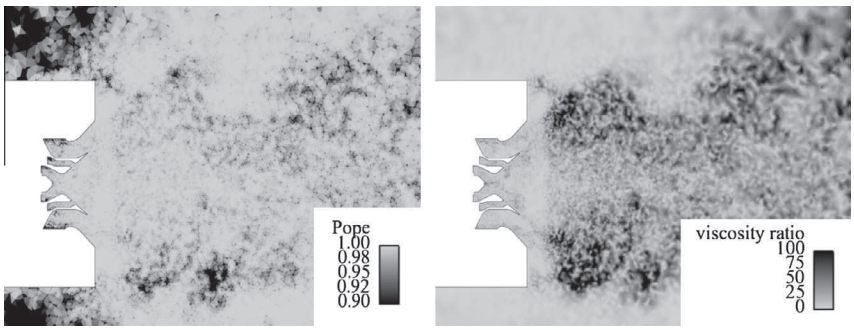


**Fig. C.27.** Snapshots of ratio of turbulent over laminar viscosity and Pope criterion, Eq. (A.1), for LES basic of Section 4.

Note also that the flows in the full swirler case (Figs. C.9 and C.10) are similar to the flows in the adjustable swirler case (Figs. C.15 and C.16), showing that replacing the full swirler computation by an equivalent set of boundary conditions has a limited impact on the flow organization, as long as both jets are in the same state (AJ or BB).

Various phenomena control the flow topology: the jet separation from the smooth curved walls of the nozzle/diffuser (Fig. C.17), the jet attachment to the side walls (Fig. C.18), the jet expansion angle due to swirl and the presence/absence of a central coherent vortex core. The jet of the basic LES computation separates more upstream and reattaches more downstream in the nozzle than the jet of the high LES case (Fig. C.17). Similarly, it detaches from the side walls earlier than the jet of LES high (Fig. C.18). How the jet separation affects the formation of a central coherent vortex core and how swirl (that is the control parameter of the system as a whole) plays a role in each of these phenomena is difficult to estimate for such complex flows and was left for further studies. However, it is important to underline that to capture all these phenomena a very fine mesh LES is required: the swirl level of the jet can be strongly affected by a poor grid at the end of the swirler vanes (as shown in Section 3 of this paper) and the detachment dynamics of the jet from the nozzle walls can be very sensitive to wall friction (which is strongly dependent on the grid resolution).

In order to verify if hysteresis is present, a second set of tests is performed by changing continuously the swirl number of the radial jet while the amount of swirl of the remaining co-axial jets is kept constant at $S = 0.12$ and $S = -0.4$ respectively. LES are cast in two groups named path A and B. Path A begins with LES basic and the following simulation is obtained by increasing the swirl number of the radial swirler jet. Path B begins with LES high and the following simulations are obtained by decreasing the swirl number of the radial swirler jet except for the final simulation ($P3\_D$) in which the swirl level is brought back to LES basic ($S = 0.75$). The investigation is limited to the range $0.6 < S < 0.84$, around the working condition of $S \approx 0.75$, which is of interest for the present study and which is sufficient to close the hysteresis loop. Paths A and B are summarized in Table C.5, while the swirler transition map is shown in Fig. C.19. The swirler bifurcation diagram (Fig. C.19) differs from the Vanierschot et al. one (Fig. C.3): this does not come as surprise since each transition map is dependent on the particular flow and geometry examined (as made evident in Vanierschot and Van den Bulck [20], who analyzed the influence of the nozzle geometry on the bifurcation diagram of their original experiment [1], presented in Section 2).

LES along path A are characterized by multiple bifurcations. At a swirl number of the radial swirler jet of 0.84 (simulation P1_U) the jet bifurcates from AJ to a flow state very similar to the "Weak axial Jet" (WJ) state described in Section 2. Differently from the Vanierschot's experiment [1], this flow state is unstable and transitory: after a period of 0.05 [s] the flow bifurcates to the BB state. Transitions change pressure and turbulence intensity distributions (Fig. C.20) as well as the shape of the CTRZ (Fig. C.21) which expands both radially and axially after each bifurcation.

Viceversa, a decrease of the swirl number of the radial swirler jet from the value of 0.84 triggers a transition in LES of path B only at $S = 0.60$ (simulation $P2\_D$): at this swirl level the jet detaches from the external side walls and bifurcates back to the AJ state (Figs. C.21 and C.22).

The adjustable swirler case results, summarized in Fig. C.19, show that the aeronautical swirler flow field with a swirl number of the radial jet close to 0.8 is close to multiple bifurcations (AJ–WJ, WJ–BB, BB–AJ) around the nominal working conditions. Two stable flow states (AJ–BB) can appear as a function of the swirl level of the jet and the initial conditions. Note that results of Fig. C.19 cannot be validated experimentally since any change of swirl level would require a total change of the swirler geometry. However, they prove that, for fixed numerical settings, the jet is very sensitive to small variations of the fluid dynamics conditions.

Results obtained in the adjustable swirler case are consistent with results of the full swirler configuration. They show that the swirl number of the radial jet of the full swirler case (0.74–0.82) is very close to the bifurcation threshold obtained in the adjustable swirler case: between $0.75 < S < 0.84$, the flow is bistable. LES senses this property and becomes sensitive to multiple parameters such as grid refinement or SGS model. As a result, characterizing swirling flows using LES can become difficult when the flow is in such conditions.

## 5. Conclusions

The present work has shown that LES of industrial swirling jets can be an extremely difficult task since small flow modifications can trigger large flow re-configurations near critical flow conditions. In the case examined here, the main parameter controlling the flow state is the swirl level of the radial jet. Bifurcations occur when swirl is changed by modifying inlet conditions or when it is changed by a modification of the LES grid or SGS model. This hypothesis was verified using a high-fidelity LES to simulate an adjustable swirl device capable of changing the amount of swirl in the flow. These bifurcations, which appeared to be due to uncontrollable errors in LES, were reproduced in a controlled environment where swirl was varied continuously. Two flow states were obtained and characterized based on the strength of the central, coherent, turbulent, vortex core associated with vortex breakdown. They are: a "free Axial Jet" (AJ) in which the central vortex core is not (or only weakly, like in simulation basic of Section 4) influenced by the presence of confinement and behaves like a free swirling jet; a "Blasted Breakdown jet" (BB), in which the central vortex core, made evident by high tangential velocity and turbulence intensity, has disappeared (or "blasted"). A third flow state, a "Weak axial Jet" (WJ) in which the central vortex core is weaker because of a jet expansion angle higher than the one of a free Axial Jet under the same amount of swirl, appeared as an unstable, transient state with the flow bifurcating either to the AJ or to the BB state for long simulation times. Flow states show similar properties in LOTAR and in the reference case of Vanierschot and Van den Bulck [1] and appear to be the result of the combination of swirl intensity and jet separation/attachment to the diverging nozzle and side walls.

A second useful consideration is that, because of hysteresis, a change in simulation parameters should be accompanied by a re-initialization of the flow field. More generally, LES for swirled flows with combustion are also very likely to exhibit bifurcating behaviors. Since combustion can act as a triggering mechanism for bifurcations and instabilities, LES codes used to study turbulent swirled confined flames should be expected to exhibit a sensitivity to numerical "detail" (similarly to what shown in this paper) which is much larger than what has been observed in non swirling free flames and might raise significant difficulties.

## Acknowledgments

The authors thank Dr. G. Staffelbach and Dr. O. Vermorel for maintaining and supporting the LES code AVBP and Dr. V. Moureau for maintaining and supporting the LES code YALES2. The support of the Marie Curie program MYPLANET (contract PITN-GA-2008-210781) is gratefully acknowledged.

## Appendix A. Mesh and LES quality

The mesh used for the adjustable swirler case of Section 4 is shown in Figs. C.23 and C.24. The mesh is fully tetrahedral and composed by 30 millions elements. The cell size gradation (variation of the cell size in neighbor elements) has been limited to 1.6. The smallest cells are located at the solid boundaries where a minimum cell size of 50 [μm] is imposed, while, inside the swirler, elements size varies between 300 [μm] and 400 [μm] (Fig. C.23). The mesh is then smoothly coarsened away from the swirler (Fig. C.24).

LES quality is assured by monitoring multiple sensors: the wall distance nondimensionalized by the boundary layer thickness, the $y^+$ values, the ratio between laminar and turbulent viscosity and the Pope criterion [2] (ratio of resolved turbulent kinetic energy to resolved plus SGS turbulent kinetic energy, Eq. (A.1)). In the adjustable swirler case, the values of $y^+$ (evaluated at the cell baricentrum) are below 10 everywhere except downstream of the swirler vanes because of the high jet velocity (Fig. C.25) while in the full swirler case they are higher (Fig. C.26).

The ratio of turbulent to laminar viscosity is low (Fig. C.27 right and Fig. C.28 up), while the Pope criterion [2]:

$$Pope = \frac{k_{res}}{k_{res} + k_{sgs}}, \tag{A.1}$$

is everywhere higher than 0.9 in the proximity of the swirler and equal to 1 inside the well resolved jet (Fig. C.27 left and Fig. C.28 down). Resolved turbulence, $k_{res}$, is evaluated as $\frac{1}{2}\sum_{i=1}^{3}(u_i'^2)$ where $u_i'$ is the Reynolds decomposition of the velocity component $u_i$. Subgrid scale turbulence is evaluated as [21]:

$$k_{sgs} = \left(\frac{v_t}{C_M \Delta}\right)^2, \tag{A.2}$$

where $C_M = 0.069$ and $\Delta$ is estimated as the cubic root of the elements volume.

## Appendix B. LES solvers and settings

All simulations of the present work are performed using the compressible LES solver named AVBP [8,9] and the incompressible LES solver named YALES2 [10]. AVBP is a finite-volume/elements solver, cell-vertex (i.e. variables are stored at nodes while conservation laws are integrated inside the elements). YALES2 is a finite-volume solver, vertex centered (equations are solved at the element vertex), 4th-order accurate in space. The numerical scheme chosen for time advancement is Lax Wendroff for AVBP while is TRK4 [22], for YALES2. TRK4 (or TFV4A) is a fourth order (time integration scheme providing a large region of stability (in terms of the Courant-Friedrichs-Lewy, CFL, number) which gives the possibility to adjust the incorporated) numerical diffusion [22]. The CFL number chosen for the current study is 0.9 for YALES2 and 0.7 (acoustic CFL number) for AVBP. Both solvers use classical LES models. For example, turbulent viscosity is expressed as:

$$v_{SGS} = (C_m \Delta)^2 D_m(\tilde{u}), \tag{B.1}$$

so that $v_{SGS}$ is proportional to the square of the grid size per an ad hoc coefficient multiplied a "differential operator associated with the model" $D_m(\tilde{u})$ [17]. The SGS model chosen for the current study is SIGMA [17], whose differential operator (i.e. turbulent viscosity coefficient) "goes to zero in near-wall regions in order to mimic the turbulence damping due to the no-slip condition" [17] (turbulent stress should decay as "the distance to the solid boundary to the third power" [17,23]) and vanishes in the case of a flow in solid rotation and in the case of a pure shear. These properties are of importance since the flow under examination in the present study is both confined and swirled.

## References


[1] Vanierschot M, Van den Bulck E. Hysteresis in flow patterns in annular swirling jets. Exp Therm Fluid Sci 2007;31(6):513–24. http://dx.doi.org/10.1016/j.expthermflusci.2006.06.001.

[2] Pope SB. Turbulent flows. Cambridge Press; 2000. ISBN:9780521598866.

[3] Faler JH, Leibovich S. Disrupted states of vortex flow and vortex breakdown. Phys Fluids 1977;20(9):1385–400. http://dx.doi.org/10.1063/1.862033.

[4] Billant P, Chomaz J-M, Huerre P. Experimental study of vortex breakdown in swirling jets. J Fluid Mech 1998;376:183–219. http://dx.doi.org/10.1017/S0022112098002870.

[5] Lucca-Negro O, O'Doherty T. Vortex breakdown: a review. Prog Energy Combust Sci 2001;27:431–81. http://dx.doi.org/10.1016/S0360-1285(00)00022-8.

[6] Cassidy John J, Falvey Henry T. Observations of unsteady flow arising after vortex breakdown. J Fluid Mech 1970;41(4):727–36. http://dx.doi.org/10.1017/S0022112070000873.

[7] Hall MG. The structure of concentrated vortex cores. Prog Aerospace Sci 1966;7:53–110. http://dx.doi.org/10.1016/0376-0421(66)90006-6.

[8] Rudgyard M, Schoenfeld T, Struijs R, Audemar G, Leyland P. A modular approach for computational fluid dynamics. CERFACS report; 1995.

[9] Rudgyard M. Integrated preprocessing tools for unstructured parallel CFD applications. CERFACS report; 1995.

[10] Moureau V, Domingo P, Vervisch L. Design of a massively parallel CFD code for complex geometries. CR Mec 2011;339(2-3):141–8. http://dx.doi.org/10.1016/j.crme.2010.12.001.

[11] Bismes F, Simon F, Gajan P, Apeloig J. Experimental characterization of the injector. Kiai deliverable d2.3.1; 2011.

[12] Gupta AK, Lilley DG, Syred N. Swirl flows. Abacus Press; 1984.

[13] Chedaille J, Leuckel W. AK Chesters aerodynamic studies carried out on turbulent jets by the international flame research. J Inst Fuel 1966;39(311):506–21.

[14] Beer JM, Chigier NA. Combustion aerodynamics. Krieger 1983.

[15] Vanierschot M, Persoons T, Van den Bulck E. A new method for annular jet control based on cross-flow injection. Phys Fluids 2009;21(2). http://dx.doi.org/10.1063/1.3037343.

[16] García-Villalba M, Fröhlich J, Rodi W. Identification and analysis of coherent structures in the near field of a turbulent unconfined annular swirling jet using large eddy simulation. Phys Fluids 2006;18(5). http://dx.doi.org/10.1063/1.2202648.

[17] Nicoud F, Baya Toda H, Cabrit O, Bose S, Lee J. Using singular values to build a subgrid-scale model for large eddy simulations. Phys Fluids 2011;23(8). http://dx.doi.org/10.1063/1.3623274.

[18] Germano Massimo, Piomelli Ugo, Moin Parviz, Cabot William H. A dynamic subgrid-scale eddy viscosity model. Phys Fluids 1991;3(7):1760–5. http://dx.doi.org/10.1063/1.857955.

[19] Wang S, Yang V, Hsiao G, Hsieh SY, Mongia HC. Large-eddy simulations of gas-turbine swirl injector flow dynamics. J Fluid Mech 2007;583:99–122. http://dx.doi.org/10.1017/S0022112007006155.

[20] Vanierschot M, Van den Bulck E. Influence of the nozzle geometry on the hysteresis of annular swirling jets. Combust Sci Technol 2007;179(8):1451–66. http://dx.doi.org/10.1080/00102200601147856.

[21] Sagaut P. Large eddy simulation for incompressible flows. Springer; 2006.

[22] Kraushaar M. Application of the compressible and low-mach number approaches to large-eddy simulation of turbulent flows in aero-engines. Phd. thesis, CERFACS 2011.

[23] Chapman Dean R, Kuhn Gary D. The limiting behaviour of turbulence near a wall. J Fluid Mech 1986;170:265–92. http://dx.doi.org/10.1017/S0022112086000885.